J Mater Sci: Mater Electron (2017) 28:8601–8610
DOI 10.1007/s10854-017-6584-4

Microwave absorption and infrared emissivity of helical polyacetylene@multiwalled carbon nanotubes composites

Wenlu Pan[1] · Man He[1] · Xiaohai Bu[2] · Yuming Zhou[1] · Binbin Ding[1] · Tingyuan Huang[1] · Shuang Huang[1] · Shiwei Li[1]

Received: 7 December 2016 / Accepted: 14 February 2017 / Published online: 24 February 2017

Abstract Hybrids of polyacetylene (PA) with multiwalled carbon nanotubes (MWNTs) were fabricated by wrapping PA derivatives containing stigmasterol and pivalic acid moieties onto MWNTs walls. The PA derivatives with moderate molecular weights ($M_n \sim 24409$) were proved to adopt a single-handed helical structure stabilized by asymmetric hydrogen bonding force and stereo-hindrance effect. Convincing experimental results show that PA had been wrapped evenly on the surface of MWNTs without damaging their internal structures. Moreover, the helical structure of PA became more compact and ordered after wrapping around MWNTs. The incorporation of stigmasterol moieties could contribute to enhancing the microwave absorbing properties and decreasing infrared emissivities. PA@MWNTs showed a minimum reflection loss value of −20.65 dB at 9.7 GHz and the bandwidth of reflection loss less than −10 dB (90% absorption) was 3.2 GHz. Meanwhile, PA@MWNTs composites had a much lower infrared emissivity value ($\varepsilon = 0.503$) than raw MWNTs. The efficient microwave absorption and low infrared emissivity might result from the synergistic effect of the extraordinary helical structure of PA and π-electronic interactions between the organic substituents and inorganic MWNTs walls, which provides a promising method to prepare materials with low infrared emissivities and excellent microwave absorption properties.

1 Introduction

Stealth technology has been widely used in military field to make targets less visible and even ideally invisible by detection equipment. Various materials with low infrared emissivity have been reported so far, such as magnetic composite [1, 2], nanofibrous membranes [3, 4], metallic thin films [5, 6], conductive polymers [7, 8], and inorganic/organic nanocomposite [9, 10]. However, with the rapid development of detection technologies, stealth materials with low infrared emissivity and high microwave absorption capacity are in desperate need. The infrared stealthy materials require high reflectance and low infrared absorption, while microwave absorbing materials are required of highly effective microwave absorption performance. To meet the requirements of compatibility, the conflicting demands for infrared and microwave camouflaged materials should be overcome. Typically, two technical ways are adopted to achieve the anticipated purpose. One way is to develop compatible stealth materials through improving the low infrared emissivity materials or microwave absorbing materials [11–13]. The other way is to coat a microwave absorbing layer with low infrared emissivity materials [14, 15]. Whereas, these reported composites still have high emissivity and their microwave absorptive capacity may decrease in wider frequency field. In-depth research on the design and synthesis of novel nanocomposites with both low infrared emissivity and high microwave absorption efficiency should be carried out.

Electronic supplementary material The online version of this article (doi:10.1007/s10854-017-6584-4) contains supplementary material, which is available to authorized users.

✉ Yuming Zhou
fchem@163.com

[1] Jiangsu Optoelectronic Functional Materials and Engineering Laboratory, School of Chemistry and Chemical Engineering, Southeast University, Nanjing 211189, China

[2] School of Materials Science and Engineering, Nanjing Institute of Technology, Nanjing 211167, China

According to recent observations, carbon materials, including carbon foams [16], carbon fibers [17] and carbon nanotubes (CNTs) [18] have aroused intensive interest in the exploitation of microwave absorbing materials. Carbon materials can provide high specific surface areas and superior congenital structures to achieve optimal dielectric and magnetic loss, thus becoming the promising building block for investigating new absorbing materials. Plenty of metal-based materials have been investigated extensively as microwave absorbers as well [19, 20]. Structural metal materials, such as nanoneedle-like ZnO (ZnOn) [21], ring-like NiO nanoparticles [22] and 3D nickel chain nets [23], exhibit tuning absorption capacity in a harsh thermal environment, which have been applied in the field of microwave device and absorber. The Carbon materials have been reported to hybridize with $CoFe_2O_4$ [24], CdS [25], Fe_3O_4/Au [26] etc. to enhance electromagnetic shielding. However, it is still quite necessary to acquire practical microwave absorbers, which possess high-efficiency, broad frequency, and lightweight. In recent years, explorative efforts have been made to the investigation of composites comprising of polymer matrix and carbon materials, aiming to obtain excellent electromagnetic shielding performance. Polypyrrole grafted Fe_3O_4 were blent with carbon nanotube to prepare Fe_3O_4/PPy/CNT composites [27], which exhibited the minimum reflection loss of −25.9 dB. Polycarbonate films containing different mass fraction of carbon nanotubes have been reported to show wide fluctuations in reflection loss values [28]. Pallab et al. fabricated a novel Gr/Ti@CNT/Fe_3O_4/PANI composite with excellent microwave absorption capacity and electrochemical property [29]. However, these reported nanocomposites still have not well resolved the disadvantages of narrow-frequency bandwidth electromagnetic interference. They were endowed with unique characteristics only in 2–18 GHz band. In addition, high loadings of metallic materials in carbon materials inevitably bring about serious processing difficulties and disadvantaged mechanical properties. Hence, there are still formidable challenges to prepare non-metallic microwave absorption composites.

Polyacetylene (PA) derivatives are representative π-conjugated polymers. Polyacetylenes with multiple functionalities can be generated by attaching appropriate functional pendants to the conjugated polyene backbones [30–32]. Especially, the introduction of chiral groups could exert asymmetric noncovalent bond forces to induce PA to form well-regulated helical structures like most natural spiral macromolecules. The symmetry of PA can be changed by intra- and intermolecular interactions, thus inducing single-handed helical conformation. It has been reported that an ordered molecular structure and hydrogen bonding in optically active polymer significantly contribute to the decrease in infrared emissivity [33, 34]. The existence of hydrogen bonding highlights the superior stealth properties of helical polymers in infrared wavelengths. The hybridization of helical polymers and carbon materials can pave the way for the fabrication of materials with low infrared emissivities and efficient microwave absorption properities. Herein, we designed and synthesized a novel polyacetylene, in which stigmasterol and *tert*-pentyl units were attached to the side chain. Stigmasterol units can provide chiral centers while achiral *tert*-pentyl units facilitate adjusting the spiral structure. The insertion of stigmasteryl moieties plays an important role in promoting the surface adhesive forces between PA and nanotube walls. The efficient electron transfer between cycloparaffins in stigmasteryl moieties and MWNTs walls make it easy to realize spontaneous wrapping. Moreover, the bulky pendants will be conducive to extend conducting pathways to enhance the conductivity of the composite. Indeed, the presence of a wider conducting network significantly influences the complex permittivity and complex permeability, thus balancing the impedance matching associated with microwave absorption process. The interface interaction is one of the key factors to increase the microwave absorption performance. It is envisioned that the PA skeleton and MWNT walls work cooperatively and the "additive effect" of electron migration can evidently improve microwave absorption while retaining low infrared emissivity.

2 Experimental section

2.1 Materials

Stigmasterol, succinic anhydride, 4-(dimethylamino)pyridine, pivalic acid, propargylamine, isobutyl chloroformate and 4-methymorpholine were purchased from Aladdin Industrial Corporation. The rhodium zwitterion catalyst (nbd)$Rh^+[\eta^6\text{-}C_6H_5B^-(C_6H_5)_3]$ (nbd = 2,5-norbornadiene) was prepared as reported [35]. Chloroform was distilled over $CaCl_2$ prior to use. MWNTs (length 5–15 μm, diameter 40–60 nm, purity>98%) were purchased from Shenzhen Nanotech Port Co., Ltd.

2.2 Measurements

FT-IR spectra were recorded on a Bruker Tensor 27 FT-IR spectrometer. ^{1}H NMR spectra were measured on a Bruker AVANCE 300 NMR spectrometer. GPC measurements were measured on a Shodex gel permeation chromatography system. Microscopic Raman spectroscopy was obtained using a DXR Raman Microscope (Thermo Fisher Scientific Inc.). XPS data were measured on a Shimadzu (Amicus, Japan) instrument. UV–vis spectra were determined with a Shimadzu UV-3600 spectrometer. CD spectra

recorded on a JascoJ-810 spectropolarimeter with a 10 mm quartz cell. Specific rotations ($[\alpha]_D$) were obtained using a WZZ-2S(2SS) digital polarimeter. TEM images were obtained on a JEM-2100 microscope. XRD measurements were performed using a Rigaku D/MAX-R. Infrared emissivity values of synthesized samples were measured on an IRE-2 Infrared Emissometer of Shanghai Institute of Technology and Physics using a silicon substrate. The electromagnetic parameters in the frequency range of 2–18 GHz were investigated by Agilent PNAN5224A vector network analyzer. The synthesized products were homogeneously blending with a paraffin matrix, which were finally pressed into toroidal-shaped samples (Φ_{out}: 7.0 mm, Φ_{in}: 3.04 mm).

2.3 Synthesis of PA copolymer

Monomer 1 is a new compound, and the typical synthesis of M1 is described below. Stigmasteryl hemisuccinate (3.2 g, 6.3 mmol), which was synthesized as reported [36], isobutyl chloroformate (0.83 mL, 6.3 mmol) and 4-methymorpholine (7.0 mL, 6.3 mmol) were sequentially dissolved in 40 mL THF, and then propargylamine (0.383 g, 6.9 mmol) was added into the solution. The mixture was stirred at room temperature for 24 h. Next, the solution was filtered off and chloroform (ca.50 mL) was added to the collected filtrate to extract the desired product. The filtrate was subsequently washed thrice with 1 M HCl, once with saturated $NaHCO_3$. The solution was dried over anhydrous $MgSO_4$ and concentrated by rotary evaporation. The crude product was recrystallized in a mixture of chloroform and *n*-hexane to obtain solid monomer. *N*-propargylamide monomers derived from *n*-pentanoic acid (M2) were synthesized according to previous papers [37].

Polymerizations were carried out with $(nbd)Rh^+[\eta^6\text{-}C_6H_5B^-(C_6H_5)_3]$ as catalyst. The monomers and catalyst were mixed in dry $CHCl_3$ ([M1] = 90 mM, [M2] = 10 mM, [catalyst] = 1 mM) under nitrogen and stirred at 30 °C for 24 h. After polymerization, the resultant solution was poured into a large amount of acetone/hexane (3/1, v/v) to precipitate the formed polymers. The precipitate was collected by filtration and dried under reduced pressure. The spectroscopic data of M1, M2 and PA are shown as follows:

M1: white solid powder. $[\alpha]_D = 20°$ (c = 0.05 g dL^{-1}, $CHCl_3$, r. t.). FT-IR (cm^{-1}, KBr): 3432, 3259(H—C≡C), 2934, 1721(C═O, ester), 1643(C═O, amide), 1537(C—N—H), 1421, 1184(C—O—C), 1062, 970, 801, 697. ^{1}H NMR (300 MHz, $CDCl_3$): δ = 0.69–2.03(43 H), 2.22(1 H, H—C≡C), 2.32(2 H), 2.48(2 H, CH_2—COO), 2.65(2 H, CH_2—C═O), 4.04(2 H, CH_2—NH), 4.62(1 H, >CH—OOC), 5.01(1 H, CH═CH), 5.14(1 H, CH═CH), 5.37(1 H, CH═C), 5.88 (1 H, N—H).

M2: white crystal. $[\alpha]_D = 5°$ (c = 0.05 g dL^{-1}, $CHCl_3$, r. t.). FT-IR (cm^{-1}, KBr): 3318(N—H), 2969, 1641(C═O), 1529, 1419, 1364, 1260, 1211, 1009, 923, 654, 558, 471. ^{1}H NMR (300 MHz, $CDCl_3$): δ = 1.23–1.64[9 H, —$C(CH_3)_3$], 2.25(1 H, CH≡C), 4.06(2 H, CH≡C—CH_2), 5.77(1 H, N—H).

PA: $M_n = 24{,}409$, $M_w/M_n = 2.1$. $[\alpha]_D = 120°$ (c = 0.05 g dL^{-1}, $CHCl_3$, r. t.). FT-IR (cm^{-1}, KBr): 3424, 2963, 1735, 1639, 1535, 1457, 1382, 1205, 1171, 1088, 968, 799, 659; ^{1}H NMR (300 MHz, $CDCl_3$): δ = 0.70–2.01 (43 H), 2.30 (2 H), 2.57 (4 H, CH_2COO, CH_2C═O), 2.84–3.0 [9 H, —$C(CH_3)_3$], 3.68–4.66 (3 H, >CH—OOC, CH_2—NH), 5.04 (1 H, CH═CH), 5.14 (1 H, CH═CH), 5.34 (1 H, CH═C), 6.08 (1 H, N—H).

2.4 Preparation of PA@MWNTs nanocomposites

The PA@MWNTs nanocomposites were prepared by solution casting. PA (10 mg) and MWNTs (20 mg) were dissolved and dispersed into 5 and 15 mL of chloroform, respectively. The two solutions were blended and sonicated with a BG-01 ultrasonic generator for 6 h. Then, the mixture was poured into a glass dish and kept for 3 days at room temperature for solvent evaporation. Finally, the obtained composites were dried under a vacuum oven at 50 °C for 24 h. The mass fraction of PA was designed as 33%.

3 Results and discussion

3.1 Characterization of PA copolymer

The synthetic route of PA is shown in Scheme 1. Monomer 1 is designed and synthesized by linking stigmasteryl moieties with propargylamine in order to introduce chiral carbon atoms into the side chain. The bulky chiral groups exert asymmetric noncovalent bonding forces to induce inerratic helical structures. The achiral M2 is introduced to copolymerize with M1 with the hope that the steric effects between the substituents will be weakened moderately and the copolymers could form inerratic helical structures. The monomers were readily polymerized in distilled $CHCl_3$ to produce PA with moderate molecular weight ($M_n \sim 24{,}409$) and appropriate molecular weight polydispersity ($M_w/M_n = 2.1$). As presented in Fig. S1, the disappearance of the chemical shift at about 2.2 ppm which is assigned to the acetylene proton in PA main chain indicates that the monomers had been consumed by the polymerization reaction. The specific rotation $[\alpha]_D$ of PA measured in chloroform at room temperature is 120°, indicating the presence of chiral amplification. Furthermore, the results based on UV–Vis and CD spectroscopic analysis (Fig. 4) are discussed below, which provide powerful evidence for the assumption that the copolymers could adopt helical structures.

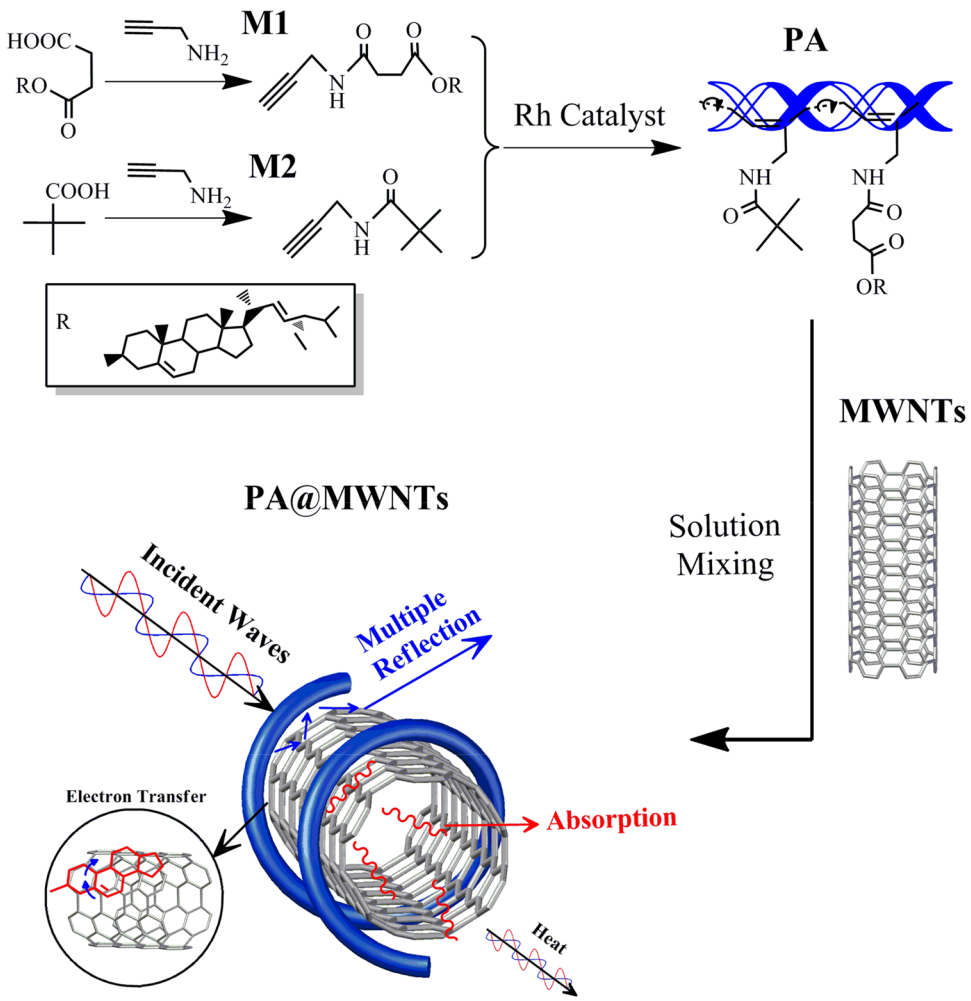

Scheme 1 Schematic illustration of synthesis of PA@MWNTs complexes

3.2 Characterization of PA@MWNTs nanocomposites

To date, the preprocessing portion of CNTs has become a starting step for the fabrication of polymers/CNT composites, such as the horizontally aligned CNT films [38], PDA functionalized CNTs [39] and UV/O_3 treatment of CNTs [40]. In this work, we display a more simplified method as compared to reported hybridization strategies of preparing CNTs-based materials. PA carrying stigmasteryl moieties showed high dispersing power in $CHCl_3$, thus significantly enhancing the dispersibility of pristine MWNTs. The non-covalent surface interactions between organic polymer and inorganic nanotubes were readily performed via sonication in $CHCl_3$ for hours. Stigmasterol functionalized PA provides polycyclic skeletons which are expected to enhance the electrostatic attraction with MWNTs walls, thus leading to stronger surface adhesive forces. In addition, MWNTs exhibit a particular sidewall curvature and inherent charge transport properties, being able to interact with naphthenes in stigmasteryl moieties through π–π electronic interactions [41]. The electron interactions can lead to a helical wrapping of conjugated backbone around individual MWNT [42], which is conducive to a smooth wrapping with a fixed diameter. The incident waves may partially penetrate the surfaces and enter into the inner cylinder, which can lead to multiple reflections in core–shell interface and attenuation by scattering or dissipating as heat. Trapped energy within the nanostructure is hard to escape until being absorbed. The schematic representation is shown in Scheme 1.

Figure 1 shows the FT-IR spectra of MWNTs, PA and PA@MWNTs. In the spectrum of PA, the peaks around 2920 cm^{-1} are relevant to the stretching vibrations of ─CH_3 and >CH_2 groups. The obvious peaks at 1735 and 1648 cm^{-1} represent C═O stretching of ester and amide groups, suggesting that side chains containing stigmasteryl moieties have been attached to PA backbone. In addition, the absorption peaks at 1535 and 1172 cm^{-1} respectively correspond to the C─N─H and C–O–C stretching vibrations which further confirm the predicted structure of PA. Interestingly, obvious blue-shifts of the absorption bands corresponding to C═O stretching of ester and amide groups

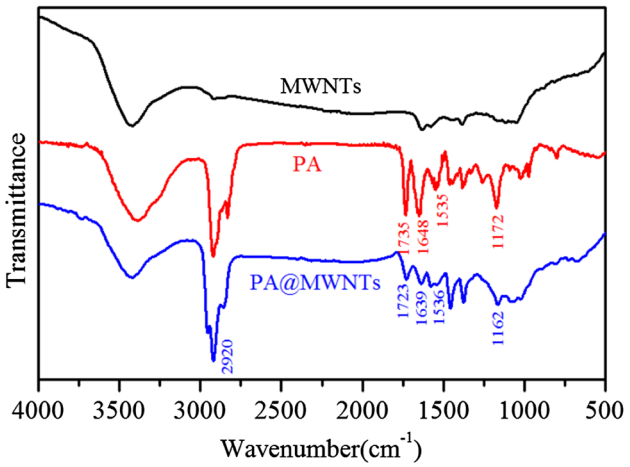

Fig. 1 FT-IR spectra of MWNTs, PA and PA@MWNTs

are observed in the spectrum of PA@MWNTs. The peak of C═O (ester) stretching shifts from 1735 to 1723 cm^{-1} while the peak of C═O (amide) stretching shifts from 1648 to 1639 cm^{-1}. It can be inferred that the integration of PA and MWNTs can change the vibration frequency of unsaturated groups, thus decreasing their intrinsic high infrared radiation. Moreover, the characteristic peaks assigned to C─N─H and C–O–C stretching in PA can also been seen in the spectrum of PA@MWNTs, demonstrating the presence of PA in composites. X-ray photoelectron spectroscopy (XPS) analysis is performed to investigate the elemental distribution of MWNTs and PA@MWNTs (Figure S2).

3.3 Morphology and crystalline structure analyses

TEM images of the PA@MWNTs are shown in Fig. 2. It is unambiguously observed that the radius of MWNTs increases and they are well wrapped by a lighter layer whose thickness is in the range of ~8–12 nm. This indicates that MWNTs are successfully coated with PA and show a core–shell structure. Moreover, clear lattice fringe is observed in Fig. 2C, which indicates that the original graphite structures of nanotubes remain unchanged after polymer wrapping. The organic counterpart is coated onto the surface of nanotubes rather equably, demonstrating the excellent adherence as well as strong interactions between MWNTs and PA. XRD curves of three samples are displayed in Fig. 3. It is clear that PA exhibited some diffraction peaks at 2θ = ~16° which are ascribed to the presence of alternating single/double bonds in main chains and cycloparaffin segments in side chains. For MWNTs, the diffraction pattern exhibited representative peaks at 2θ = 26.12°, 42.99°, 53.65° and 78.21°, which are assigned to (002), (101), (004), and (006) crystal-line planes in graphite structure, respectively. The characteristic

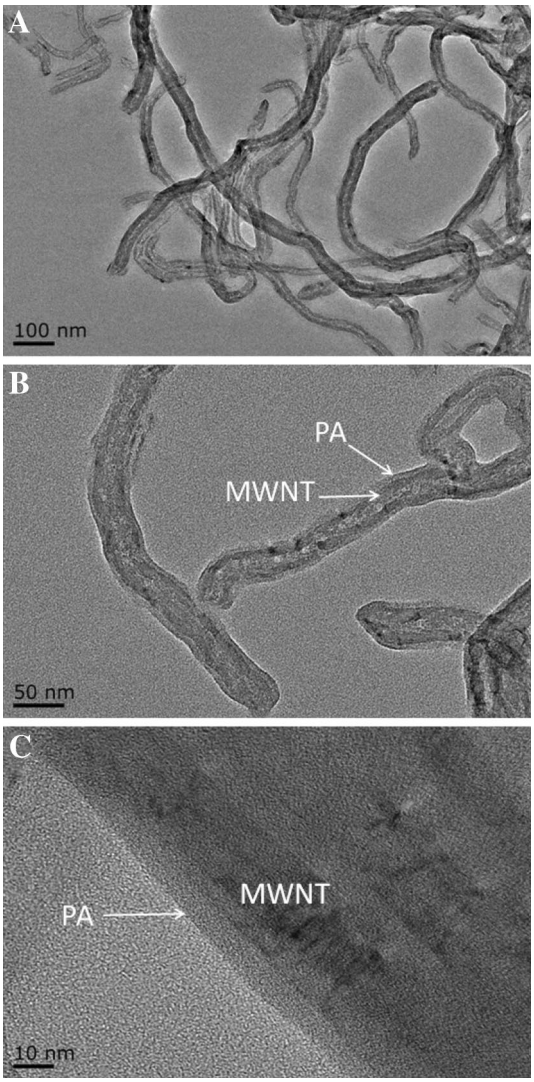

Fig. 2 TEM images of the PA@MWNTs composites

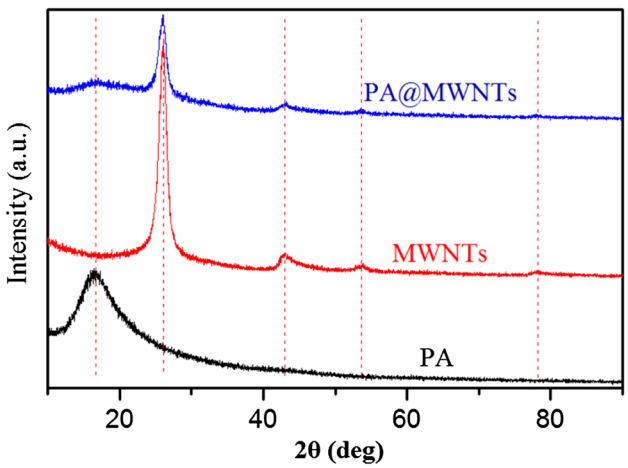

Fig. 3 XRD patterns of PA, MWNTs and PA@ MWNTs composites

diffraction peaks are still detected in the pattern of PA@MWNTs. This indicates that the incorporation of stigmasterol segments provides the space for sensing photoelectronic interactions between PA matrix and MWNTs and the organic and inorganic components are hybridized successfully without damaging the internal architectures. The peak intensities of the hybrids are much weaker than those of MWNTs and PA, which may be due to the high ratio of stereocomplex crystallites in the nanocomposites [43]. Both TEM images and XRD curves confirm that the PA chains have evenly wrapped the MWNTs.

3.4 UV–vis and CD spectra analyses

The optical activities of pristine PA and PA@MWNTs are confirmed by UV–vis and CD spectroscopies in THF. As shown in Fig. 4, the UV–vis spectra of MWNTs demonstrate a broad absorption peak from 230 to 500 nm, but the CD signal is inactive. The UV absorption spectrum of PA demonstrate the strong sharp absorption centered around 240 nm and the shoulder peak range from 250 to 350 nm, which are assigned to the combined characteristic band of the alternating single/double bonds in main chain and naphthenic structures in pendants, respectively. Meanwhile, the CD spectrum of PA shows a distinct Cotton effect at ~260 nm which is consistent with the investigation of secondary structure conformation [44], implying predominantly single-handed screw sense of PA chains.

The UV spectra of PA@MWNTs demonstrate similar medium peaks at the wavelength range from 230 to 500 nm, which are the combined characteristic bands of PA and MWNTs. Interestingly, the suspension also has a negative Cotton effect at 260 nm, which indicates that the PA still maintain considerable optical activity. In particular, the strengthened intensity of the CD signal demonstrates that the organic PA chains in the composite not only maintain helical structures, but also form more compact and ordered helixes. This is possibly caused by the π-electronic interactions between the MWNTs and the conjugated backbone of PA. The results also confirm that the hybridization of helical PA on the surface of MWNTs can improve the stability of organic macromolecule.

3.5 Microwave absorbing properties

To study the microwave absorbing properties of PA@MWNTs composites, the as-prepared samples are impregnated with paraffin wax and fabricated into toroidal-shaped samples. According to the Debye theory, the real part of permittivity (ε′) represents the stored electromagnetic energy within the medium while the imaginary part of permittivity (ε″) represents the dielectric loss [20]. The frequency-dependent ε′ and ε″ of PA, MWNTs and PA@MWNTs composites are displayed in Fig. 5a, b. We can observe that the ε′ and ε″ values of PA@MWNTs composites are between those of the pristine PA and MWNTs. Meanwhile, the ε′ values of PA@MWNTs composites fluctuate in the range of 8.3–12.8 and the ε″ values fluctuate in the range of 1.7–5.1. It is clearly seen that the ε′ values of MWNTs show a descending trend with increasing frequency, while the ε″ values experience a rising trend. In addition, the ε″ value of PA sample maintains around 0, indicative of low conductivity and low dielectric loss of PA.

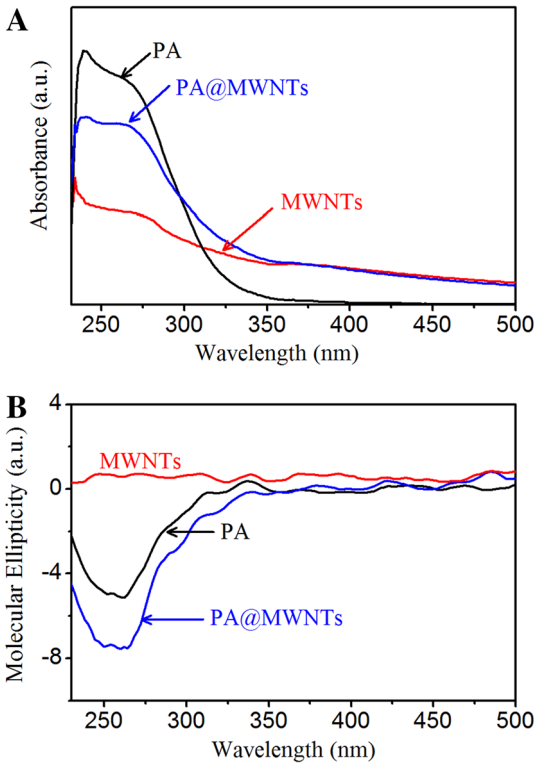

Fig. 4 **a** UV–vis and **b** CD spectra of PA, MWNTs and PA@MWNTs composites. (measured in THF, c = 0.2 mM)

We also calculated the dielectric loss tangents (tan $\delta_\varepsilon = \varepsilon''/\varepsilon'$) and magnetic loss tangents (tan $\delta_\mu = \mu''/\mu'$) of the samples, respectively. As shown in Fig. 5c, d, the dielectric loss tangents of PA@MWNTs exhibit small fluctuations, which is consistent with imaginary permittivity curve. As reported previously, the matching between complex permittivity and complex permeability the make possible contributions to microwave absorption [45, 46]. Hence, extremely high or low values of dielectric loss tangents will go against the impedance match. For PA@MWNTs composites, both conduction loss and polarization loss contribute to dielectric loss. The polarization loss can be ascribed to interfacial polarizations and dipole polarizations [25, 47]. The interfacial polarizations are caused by the abundant interfaces

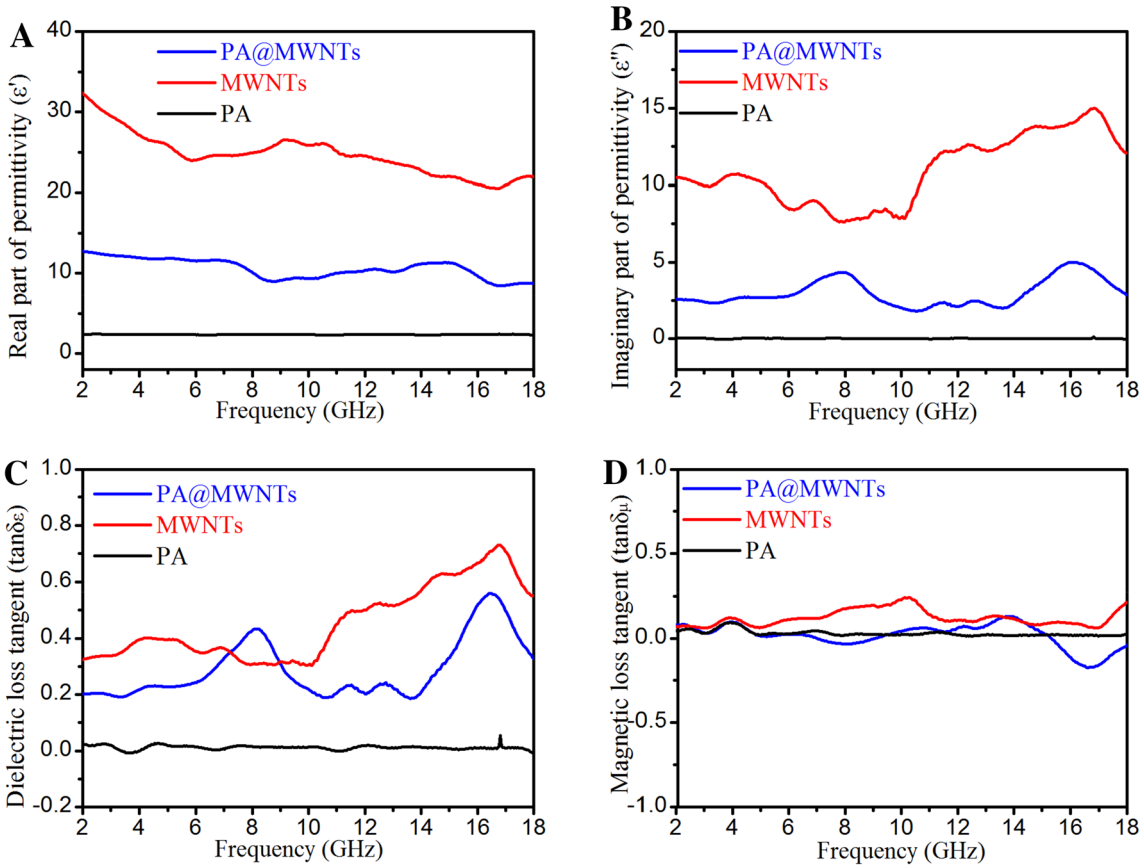

Fig. 5 Frequency dependent **a** real parts, **b** imaginary parts of the complex permittivity, **c** dielectric loss tangents and the **d** magnetic loss tangents of PA, MWNTs and PA@MWNTs. (40 wt% in paraffin wax)

between PA macromolecule and MWNT walls while the dipole polarizations originate from functional groups in PA and defects in MWNTs. It is already known that the electrical conductivity of CNT-based composites is attributed to the conductive network created by CNT aggregations. Oscillatory current can be produced in the conductive network, which accelerates the attenuation of incident electromagnetic energy [48]. However, in comparison with pure MWNTs, the electrical conductivity of the composites is lower because additional contact electrical resistance exists in the core/shell interface. As a result, the decreased imaginary permittivity of PA@MWNTs composites can be seen in Fig. 5b. In addition, due to the absence of magnetic components in the as-synthesized samples, the real and imaginary parts of complex permeability are around 1.0 and 0.0, respectively (shown in Figure S3). The magnetic loss values (tan δ_μ) of PA@MWNTs are less than the dielectric losses values (tan δ_ε), indicating that the efficient microwave absorption of PA@MWNTs are mainly attributed to dielectric loss.

The reflection loss (RL) are measured in the frequency range of 2–18 GHz. Microwave absorption properties of the samples are evaluated by the reflection loss on the basis of the transmission line theory [49, 50], which is summarized as the following equations:

$$Z_{in} = (\mu_r/\varepsilon_r)^{1/2} \tanh\left[j(2\pi fd/c)(\mu_r\varepsilon_r)^{1/2}\right] \quad (1)$$

$$RL(dB) = 20\lg\left|\frac{Z_{in}-1}{Z_{in}+1}\right| \quad (2)$$

where $Z_{in}$is the input impedance of the absorber, $\varepsilon_r$and μ_r are the relative complex permittivity and the relative complex permeability, respectively, f is the frequency, d is the thickness and c is the velocity of electromagnetic waves in free space. An ideal reflection loss (RL(dB)) is restricted by several factors including characteristic impedance, interface relaxation, dielectric loss, magnetic loss, etc [51].

Figure 6 shows the RL curves of PA, MWNTs and PA@MWNTs (40 wt% in wax) with different thicknesses (2, 2.5, 3, 3.5, 4, 4.5 and 5 mm) in the frequency range 2–18 GHz. As shown in Fig. 6a, calculated RL curves of PA sample with various thicknesses have hardly any effective reflection loss bandwidth. It is worthy to notice

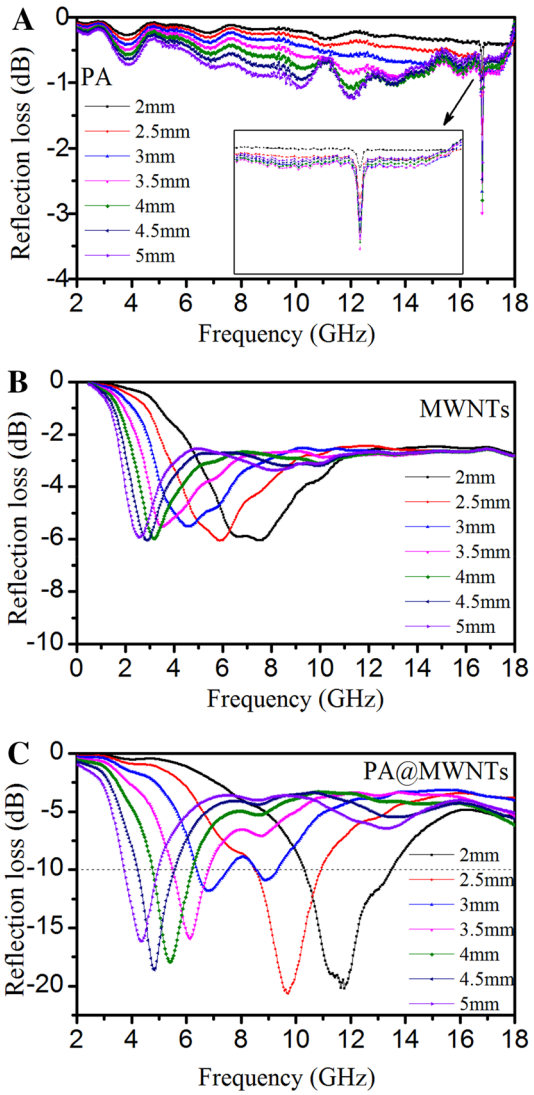

Fig. 6 Reflection loss curves of PA, MWNTs and PA@MWNTs with thicknesses of 2, 2.5, 3, 3.5, 4, 4.5 and 5 mm in the frequency range 2–18 GHz

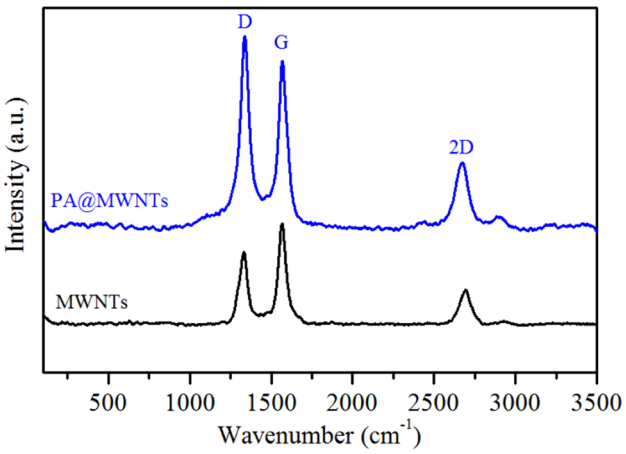

Fig. 7 Raman spectra of raw MWNTs and PA@MWNTs

that the obvious peaks at around 16.8 GHz don't shift with increasing thickness, indicative of a resonance behavior occurred between PA macromolecule and paraffin [52]. The reflection loss values of the composites decrease substantially, suggesting that PA@MWNTs composites are more efficient in microwave absorption by comparing to pristine PA and MWNTs. To be more specific, bandwidths exceeding −10 dB for the PA@MWNTs samples of 2 and 2.5 mm are 10.31–13.54 GHz and 8.52–10.92 GHz, respectively. Meanwhile, the minimum RL values are −20.22 dB at 11.79 GHz and −20.65 dB at 9.7 GHz, respectively. It should be noted that the attenuation peaks gradually shift towards lower frequency with increasing thickness, which is significantly different from the tendency of PA (shown in Fig. 6a). This indicates the successful hybridization between PA and MWNTs. Moreover, the microwave absorption properties are proved to be effectively tuned by adjusting the layer thicknesses in this framework. The phenomenon might be attributed to the fact that the thickness variation of materials would lead to different electrical conductivity and dielectric properties, thus changing the impedance matching conditions at the interface between the materials and free space [45]. Hence, they exhibit different microwave absorbing performance. Moreover, all the minimum RL values of PA@MWNTs for the thicknesses 3, 3.5, 4, 4.5 and 5 mm have decreased for a large scale compared with those of PA and MWNTs, which indicates that the hybrids meet the main requirements for microwave absorbers. The maximal effective absorption bandwidth of PA@MWNTs still reaches 3.2 GHz, broader than the reported composites based on carbon materials [53, 54].

The enhanced microwave absorption performance of PA@MWNTs might be attributed to unique nanostructures of MWNTs and multiple organic–inorganic interfacial interactions. The twisted MWNTs provide the one-dimensional nanostructures which may bring about multiple reflections of incident microwaves and trap the energy within the composites. The entered microwaves can be attenuated by scattering or dissipating as heat, which greatly contribute to decreasing the RL values. Multiple organic–inorganic interfacial interactions, including electronic redistribution behavior, can also result in the superior absorption of electromagnetic energy. As shown in Fig. 7, the samples show three similar characteristic peaks at around 1338, 1570 and 2672 cm^{-1} which represent D-band, G-band and 2D-band, respectively. However, the intensity ratio (I_D/I_G) significantly varies, where I_D/I_G ratio for raw MWNTs and PA@MWNTs is 0.69 and 1.12, respectively. The G band is correlated with the vibration of sp^2 carbon atoms while the D band indicates a hybridized vibrational

mode related to sp^3 defects. The increase in the intensity ratio (I_D/I_G) of MWNTs has been used as evidence for the destruction of sp^2 character and the formation of sp^3 defects [55, 56]. With the integration of side chains containing multiple cycloparaffin hydrocarbons, both the intensities of D band and G band increase significantly. This indicates electrons redistribution occurred between the organic macromolecule and inorganic carbon nanotubes. The electronic transport would be performed in different modes, which are described as migrating electron and hopping electron [57, 58]. Both the migration of electrons in one graphene layer and the long-distance transfer of hopping electrons between amorphous layers would influence the conductivity of the MWNTs network, thus leading to high electric loss [59]. On the other hand, the stigmasteryl groups in PA are strong electron donors, which is conducive to electron donor–acceptor (D–A) interactions between PA and MWNT walls [60]. The electrons in conjugated backbone partially jump across the energy barrier between PA and MWNTs as hopping electrons, promoting the electron transitions in heterogeneous materials. Based on the above mentioned analyses, we can conclude that unique nanostructures, interfacial interaction significantly contribute to enhancing microwave absorption performance of PA@MWNTs.

3.6 Infrared emissivity property study

The infrared emissivity values at wavelength of 8–14 μm are presented in Table 1. The PA@MWNTs has the infrared emissivity at the value of 0.503, which is much lower than the constituent parts. This may be attributed to hydrogen bonding between oxygen containing groups like C═O, O─H and –NHCO–. PA is designed to form compact helical structures where the formation of hydrogen bonding between the highly unsaturated groups could reduce the index of hydrogen deficiency and unsaturated degree [61]. The vibrational state of unsaturated bonds will be changed if more well-ordered fragments accumulate in the macromolecule, eventually facilitating the remarkable reflection of infrared ray. Besides the helical conformation, medium electron withdrawing groups like ester group and amide group also interacted with the electron donating MWNT walls. Compared with other kinds of polyacetylene, the incorporation of stigmasteryl moieties strengthens the conjugation effect of polyacetylene main chain and the π-electronic interactions between pendants and MWNTs walls. The electron transfer between nanotube shell and organic matrix alters the torsional angles and thermal restraining in backbone, thus decreasing the absorption of infrared ray. As a result, the synergistic effect of helical conformation and electron redistribution contributes to the reduction of infrared emissivity.

Table 1 Infrared emissivity values of samples at room temperature

Samples	Infrared emissivity ε_{25} (8–14 μm)
MWNTs	0.795
PA	0.619
PA@MWNTs	0.503

4 Conclusion

In conclusion, we prepared an optically active PA@MWNTs nanohybrid through noncovalent wrapping substituted polyacetylenes on the surface of MWNTs. Convincing experimental results show that the insertion of stigmasteryl moieties not only strengthens electron transfer which promotes the surface adhesive forces between PA and nanotube walls, but also facilitates adjusting the spiral structure to decrease infrared emissivity. The helical structure is more compact and ordered after the hybridization with MWNTs. The PA@MWNTs matrix can exhibit a much lower infrared emissivity as low as 0.503 at the wavelength of 8–14 μm and present ideal reflection loss ($RL_{min} = -20.65$ dB) and wide absorption bandwidths (3.2 GHz). The fabrication of PA@MWNTs composites presents a facile method for developing materials with low infrared emissivities and efficient microwave absorption.

Acknowledgements The research was financially supported by the National Nature Science Foundation of China (51673040, 21376051, 21676056 and 21306023), the Prospective Joint Research Project of Jiangsu Province (BY2016076-01), a Project Funded by the Priority Academic Program Development of Jiangsu Higher Education Institutions (PAPD) (1107047002), the Fundamental Research Funds for the Central Universities (3207046302), Fund Project for Transformation of Scientific and Technological Achievements of Jiangsu Province of China (BA2016105), based on scientific research SRTP of Southeast University (T16192020), the Scientific Research Foundation of Graduate School of Southeast University (YBJJ1417). The authors especially appreciate Nanjing University of Aeronautics and Astronautics Prof. He Jianping Group's help with VNA test.

References

1. L. Yuan, J. Hu, X. Weng, Q. Zhang, L. Deng, J. Alloy. Compd. **670**, 275 (2016)
2. X. Zhao, Y.-L. Zhang, X.-X. Wang, H.-L. Shi, W.-Z. Wang, M.-S. Cao, J. Mater. Sci. **27**, 11518 (2016)
3. X. Mao, Y. Bai, J. Yu, B. Ding, Dalton T. **45**, 6660 (2016).
4. J. Tahalyani, K.K. Rahangdale, R. Aepuru, B. Kandasubramanian, S. Datar, Rsc Adv. **6**, 36588 (2016).
5. R. Shu, H. Xing, X. Cao, X. Ji, D. Tan, Y. Gan, Nano **11**, 1650047 (2016).

6. X.-J. Zhang, G.-C. Lv, G.-S. Wang, T.-Y. Bai, J.-K. Qu, X.-F. Liu, P.-G. Yin, RSC Adv. **5**, 55468 (2015).
7. H. Li, K. Xie, Y. Pan, M. Yao, C. Xin, Synthetic Met. **59**, 1386 (2009).
8. H. Yang, N. Han, Y. Lin, P. Kang, G. Zhang, J. Wang, F. Wang, J. mater. Sci. **27**, 10849 (2016).
9. S. Fang, W. Wang, X. Yu, H. Xu, Y. Zhong, X. Sui, L. Zhang, Z. Mao, Mater. Lett. **143**, 120 (2015)
10. W. Zhou, X. Hu, X. Bai, S. Zhou, C. Sun, J. Yan, P. Chen, ACS Appl. Mater. Inter. **3**, 3839 (2011).
11. L. Chen, C. Lu, Y. Lu, Z. Fang, Y. Ni, Z. Xu, RSC Adv. **3**, 3967 (2013).
12. L. Chen, C. Lu, Y. Zhao, Y. Ni, J. Song, Z. Xu, J. Alloy. Compd. **509**, 8756 (2011)
13. X. Li, G. Ji, H. Lv, M. Wang, Y. Du, J. Magn. Magn. Mater. **355**, 65 (2014).
14. T. Wang, J. He, J. Zhou, J. Tang, Y. Guo, X. Ding, S. Wu, J. Zhao, J. Solid State Chem. **183**, 2797 (2010)
15. C.C. Yang, Y.J. Gung, W.C. Hung, T.H. Ting, K.H. Wu, Compos. Sci. Technol. **70**, 466 (2010)
16. C. Wang, Y. Ding, Y. Yuan, X. He, S. Wu, S. Hu, M. Zou, W. Zhao, L. Yang, A. Cao, Y. Li, J. Mater. Chem. C **3**, 11893 (2015)
17. G. Li, T. Xie, S. Yang, J. Jin, J. Jiang, J. Phys. Chem. C **116**, 9196 (2012)
18. L.J. Deng, M.G. Han, Appl. Phys. Lett. **91**, 3 (2007)
19. Y. Li, X. Fang, M. Cao, Sci. Rep. **6**, 24837 (2016)
20. B. Zhao, G. Shao, B. Fan, W. Zhao, Y. Xie, R. Zhang, J. Mater. Chem. A **3**, 10345 (2015)
21. J. Liu, W.-Q. Cao, H.-B. Jin, J. Yuan, D.-Q. Zhang, M.-S. Cao, J. Mater. Chem. C **3**, 4670 (2015)
22. H. Yang, M. Cao, Y. Li, H. Shi, Z. Hou, X. Fang, H. Jin, W. Wang, J. Yuan, Adv. Opt. Mater. **2**, 214 (2014)
23. J. Liu, M.S. Cao, Q. Luo, H.L. Shi, W.Z. Wang, J. Yuan, ACS Appl. Mater. Inter. **8**, 22615 (2016).
24. R.C. Che, C.Y. Zhi, C.Y. Liang, X.G. Zhou, Appl. Phys. Lett. **88**, 3 (2006)
25. M. Lu, X. Wang, W. Cao, J. Yuan, M. Cao, Nanotechnology **27**, 065702 (2016)
26. C. Liu, Y. Xu, L. Wu, Z. Jiang, B. Shen, Z. Wang, J. Mater. Chem. A **3**, 10566 (2015)
27. R.-B. Yang, P.M. Reddy, C.-J. Chang, P.-A. Chen, J.-K. Chen, C.-C. Chang, Chem. Eng. J. **285**, 497 (2016)
28. H.M. Mesfin, S. Hermans, I. Huynen, A. Delcorte, C. Bailly, Mater. Today **3**, 491 (2016).
29. P. Bhattacharya, S. Dhibar, M.K. Kundu, G. Hatui, C.K. Das, Mater. Res. Bull. **66**, 200 (2015)
30. J. Park, T. Yu, T. Inagaki, K. Akagi, Macromolecules **48**, 1930 (2015)
31. H.Y. Zhang, B.A. Zhao, J.P. Deng, Chem. Rec. **16**, 964 (2016).
32. S. Sugano, H. Kouzai, Bull. Chem. Soc. Jpn. **89**, 27 (2016)
33. Y. Yang, Y. Zhou, J. Ge, X. Yang, React. Funct. Polym. **72**, 574 (2012)
34. M. Zhang, Y. Zhou, M. He, T.Z. Tao Zhang, X. Bu, RSC Adv. **5**, 88548 (2015).
35. R.R. Schrock, J.A. Osborn, Inorg. Chem. **9**, 2339 (1970)
36. N. Vida, H. Svobodova, L. Rarova, P. Drasar, D. Saman, J. Cvacka, Z. Wimmer, Steroids **77**, 1212 (2012)
37. J. Deng, J. Tabei, M. Shiotsuki, F. Sanda, T. Masuda, Macromolecules **37**, 5149 (2004)
38. K. Krukiewicz, J.S. Bulmer, D. Janas, K.K.K. Koziol, J.K. Zak, Appl. Surf. Sci. **335**, 130 (2015)
39. Q. Wan, J. Tian, M. Liu, G. Zeng, Q. Huang, K. Wang, Q. Zhang, F. Deng, X. Zhang, Y. Wei, Appl. Surf. Sci. **346**, 335 (2015)
40. S. Roy, T. Das, Y. Ming, X. Chen, C.Y. Yue, X. Hu, J. Mater. Chem. A **2**, 3961 (2014)
41. E. Bayram, E. Akyilmaz, Sensor. Actuat. B **233**, 409 (2016).
42. A. Bar-Hen, C. Bounioux, R. Yerushalmi-Rozen, E. Gonzalez Solveyra, I. Szleifer, J. colloid Interface Sci. **452**, 62 (2015).
43. Y. Sun, C. He, RSC Adv. **3**, 2219 (2013).
44. F. Sanda, T. Fujii, M. Shiotsuki, T. Masuda, Polym. J. **40**, 768 (2008).
45. M. Cao, R. Qin, C. Qiu, J. Zhu, Mater. Design **24**, 391 (2003)
46. Z. Wang, L. Wu, J. Zhou, W. Cai, B. Shen, Z. Jiang, J. Phys. Chem. C **117**, 5446 (2013)
47. J.-Z. He, X.-X. Wang, Y.-L. Zhang, M.-S. Cao, J. Mater. Chem. C **4**, 7130 (2016)
48. M.S. Cao, J. Yang, W.L. Song, D.Q. Zhang, B. Wen, H.B. Jin, Z.L. Hou, J. Yuan, ACS Appl. Mater. Inter. **4**, 6949 (2012).
49. D. Chen, H. Quan, G.-S. Wang, L. Guo, ChemPlusChem **78**, 843 (2013).
50. D.-D. Zhang, D.-L. Zhao, J.-M. Zhang, L.-Z. Bai, J. Alloy. Compd. **589**, 378 (2014)
51. J. Joo, C.Y. Lee, J. Appl. Phys. **88**, 513 (2000)
52. Y. Wang, W. Zhang, C. Luo, X. Wu, G. Yan, W. Chen, Synthetic Met. **220**, 347 (2016).
53. Z. Liu, G. Bai, Y. Huang, F. Li, Y. Ma, T. Guo, X. He, X. Lin, H. Gao, Y. Chen, J. Phys. Chem. C **111**, 13696 (2007)
54. D.-L. Zhao, X. Li, Z.-M. Shen, J. Alloy. Compd. **471**, 457 (2009)
55. R.S. Chouhan, A. Qureshi, B. Yagci, M.A. Gülgün, V. Ozguz, J.H. Niazi, Chem. Eng. J. **298**, 1 (2016)
56. P. Khanra, T. Kuila, N.H. Kim, S.H. Bae, D.-S. Yu, J.H. Lee, Chem. Eng. J. **183**, 526 (2012)
57. B. Wen, M.-S. Cao, Z.-L. Hou, W.-L. Song, L. Zhang, M.-M. Lu, H.-B. Jin, X.-Y. Fang, W.-Z. Wang, J. Yuan, Carbon **65**, 124 (2013)
58. M.-S. Cao, W.-L. Song, Z.-L. Hou, B. Wen, J. Yuan, Carbon **48**, 788 (2010)
59. W.-L. Song, M.-S. Cao, Z.-L. Hou, X.-Y. Fang, X.-L. Shi, J. Yuan, Appl. Phys. Lett. **94**, 233110 (2009)
60. H. Zhao, W.Z. Yuan, J. Mei, L. Tang, X.Q. Liu, J.M. Yan, X.Y. Shen, J.Z. Sun, A. Qin, B.Z. Tang, J. Polym. Sci. Pol. Chem. **47**, 4995 (2009).
61. X. Bu, Y. Zhou, Z. Chen, M. He, T. Zhang, React. Funct. Polym. **82**, 17 (2014)